The Astrophysical Journal, 978:110 (16pp), 2025 January 01 https://doi.org/10.3847/1538-4357/ad9748

Finding the Fuse: Prospects for the Detection and Characterization of Hydrogen-rich Core-collapse Supernova Precursor Emission with the LSST

A. Gagliano[1,2,3], E. Berger[1,2], V. A. Villar[1,2], D. Hiramatsu[1,2], R. Kessler[4,5], T. Matsumoto[6,7], A. Gilkis[8], and E. Laplace[9]

[1] The NSF AI Institute for Artificial Intelligence and Fundamental Interactions; alexander.gagliano@cfa.harvard.edu
[2] Center for Astrophysics | Harvard & Smithsonian, Cambridge, MA 02138, USA
[3] Department of Physics, Massachusetts Institute of Technology, Cambridge, MA 02139, USA
[4] Kavli Institute for Cosmological Physics, University of Chicago, Chicago, IL 60637, USA
[5] Department of Astronomy and Astrophysics, University of Chicago, Chicago, IL 60637, USA
[6] Department of Astronomy, Kyoto University, Kitashirakawa-Oiwake-cho, Sakyo-ku, Kyoto, 606-8502, Japan
[7] Hakubi Center, Kyoto University, Yoshida-honmachi, Sakyo-ku, Kyoto, 606-8501, Japan
[8] Institute of Astronomy, University of Cambridge, Madingley Road, Cambridge CB3 0HA, UK
[9] Heidelberger Institut für Theoretische Studien, Schloss-Wolfsbrunnenweg 35, D-69118 Heidelberg, Germany

Received 2024 August 23; revised 2024 November 23; accepted 2024 November 24; published 2024 December 30

Abstract

Enhanced emission in the months to years preceding explosion has been detected for several core-collapse supernovae (SNe). Though the physical mechanisms driving the emission remain hotly debated, the light curves of detected events show long-lived ($\geqslant$50 days), plateau-like behavior, suggesting hydrogen recombination may significantly contribute to the total energy budget. The Vera C. Rubin Observatory's Legacy Survey of Space and Time (LSST) will provide a decade-long photometric baseline to search for this emission, both in binned pre-explosion observations after an SN is detected and in single-visit observations prior to the SN explosion. In anticipation of these searches, we simulate a range of eruptive precursor models to core-collapse SNe and forecast the discovery rates of these phenomena in LSST data. We find a detection rate of ∼40–130 yr^{-1} for SN IIP/IIL precursors and ∼110 yr^{-1} for SN IIn precursors in single-epoch photometry. Considering the first three years of observations with the effects of rolling and observing triplets included, this number grows to a total of 150–400 in binned photometry, with the highest number recovered when binning in 100 day bins for 2020tlf-like precursors and in 20 day bins for other recombination-driven models from the literature. We quantify the impact of using templates contaminated by residual light (from either long-lived or separate precursor emission) on these detection rates, and explore strategies for estimating baseline flux to mitigate these issues. Spectroscopic follow-up of the eruptions preceding core-collapse SNe and detected with LSST will offer important clues to the underlying drivers of terminal-stage mass loss in massive stars.

Unified Astronomy Thesaurus concepts: Sky surveys (1464); Core-collapse supernovae (304); Stellar mass loss (1613)

1. Introduction

Evidence has steadily grown that the formation of circumstellar material (CSM) regularly precedes the death of massive stars as core-collapse supernovae (CCSNe). Persistent narrow emission lines appearing in the spectra of supernovae (SNe) and caused by the photoionization of slow-moving (∼10–1000 $\mathrm{km\,s^{-1}}$; A. V. Filippenko 1997; F. Taddia et al. 2013) CSM by the SN ejecta have long suggested that at least *some* SNe do not explode into pristine environments. The most common subtype exhibiting these features, SN IIn (where the "n" stands for "narrow"; E. M. Schlegel 1990), is spectroscopically characterized by an early blue continuum and prominent Hα emission, and the class exhibits broad photometric diversity dominated by CSM interaction. Balmer emission features lasting weeks to months have also appeared in the spectra of SNe with well-defined photometric plateaus, leading to the designation of the SN IIn-P subclass (J. C. Mauerhan et al. 2013b; N. Smith 2013; M. Fraser 2020). This long-lived interaction is not limited to hydrogen-rich SNe: narrow spectral features from slow-moving CSM are also observed in hydrogen-poor SNe, including helium-rich SNe Ibn (A. Gangopadhyay et al. 2020; N.-C. Sun et al. 2020; K. Maeda & T. J. Moriya 2022; M. Pursiainen et al. 2023; Q. Wang et al. 2024) and helium-poor SNe Icn (A. Gal-Yam et al. 2022; C. Pellegrino et al. 2022; K. W. Davis et al. 2023; T. Nagao et al. 2023).

The detection of prominent emission lines above the SN photosphere requires high CSM densities, and by measuring the velocity of the post-shocked shell from intermediate-width spectral features (or by inferring the shock velocity from light curve models), mass-loss rates in the terminal progenitor system can be estimated (see N. Smith 2014, for a review). Sample studies of SNe IIn have reported progenitor mass-loss rates of 10^{-2} to $>1\,M_{\odot}\,\mathrm{yr}^{-1}$ (N. Smith 2014, 2017), far exceeding expectations for line-driven stellar winds—and ostensibly supporting an eruptive origin with unclear underlying physics. Further complicating the picture, the existence of local CSM surrounding otherwise typical SNe IIP/IIL has been more recently suggested by the presence of short-lived narrow spectral lines originating from material flash-ionized by the initial pulse of SN photons. Comprehensive searches for these flash-ionization features, paired with the timescales of observed shock breakout, indicate that dense CSM formation is a regular occurrence in CCSNe (F. Forster et al. 2018; W. V. Jacobson-Galán et al. 2024b). Stars less massive than $<30\,M_{\odot}$ likely end their lives as red supergiants (RSGs), which are not expected to exhibit eruptive, Luminous Blue Variable (LBV)-

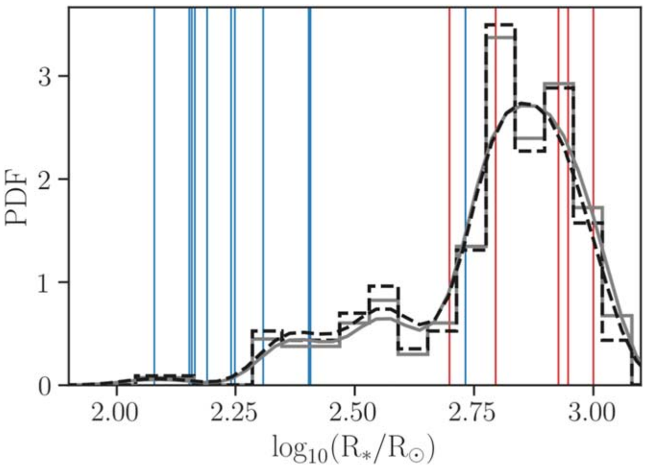

Figure 1. Progenitor radius priors for our IIP/IIL (solid gray line) and IIn (black dashed line) precursor SED grids, derived from MESA simulations of single and binary-star systems evolved to core collapse. SN II progenitors are selected by a minimum threshold on hydrogen mass at the end of the simulation, and the radii of candidate SN II progenitors in binary systems are used to construct the SN IIn prior. Gaussian kernel density estimates (overplotted smoothed curves) are made from each sample and used to weight the associated SEDs in the simulation. The inferred progenitor radii of SNe IIP 2004A, 2009ib, 2017eaw, 2017gmr (J. A. Goldberg & L. Bildsten 2020), and 2024ggi (D. Xiang et al. 2024) are shown as vertical red lines, and those inferred for Galactic Luminous Blue Variables from L. Mahy et al. (2022) using interferometry are shown as vertical blue lines.

like mass loss. Multiple mechanisms have been proposed to explain this enhanced mass loss in RSGs, including the damping of convective waves launched by changes in late-stage nuclear burning (E. Quataert & J. Shiode 2012), pulsation-driven superwinds (A. Heger et al. 1997; S.-C. Yoon & M. Cantiello 2010), and binary interaction (T. Matsuoka & R. Sawada 2024).[10]

Complementing the rapid spectroscopic follow-up that has made these discoveries possible, wide-field photometric surveys have both expanded the local discovery volume and increased the typical cadence of observations. The All-Sky Automated Survey for SNe (ASAS-SN; B. J. Shappee et al. 2014), the Asteroid Terrestrial Last-Alert System (J. L. Tonry et al. 2018), the Zwicky Transient Facility (ZTF; E. C. Bellm et al. 2019; M. J. Graham et al. 2019; F. J. Masci et al. 2019; R. Dekany et al. 2020), and the Young SN Experiment (D. O. Jones et al. 2021; P. D. Aleo et al. 2023) provide near-synoptic coverage of the sky and temporal sampling of <1 day for events serendipitously occurring in the overlap between survey footprints. This wealth of archival imaging has enabled both proactive and retroactive searches for pre-explosion emission from local SNe. This thread began with the detection of emission preceding the Type Ibn SN 2006jc (the precursor light curve is shown as the right panel of Figure 4 in R. J. Foley et al. 2007; A. Pastorello et al. 2007). The detection was followed by precursor emission detected in 2010mc (E. O. Ofek et al. 2013; light curve shown in Figure 1) 2015bh (Figure 2; C. C. Thöne et al. 2017), 2016bdu (erroneously listed as 2016bhu in A. Pastorello et al. 2018; T. Matsumoto & B. D. Metzger 2022a), LSQ13zm (L. Tartaglia et al. 2016), and 2009ip (E. Berger et al. 2009; R. J. Foley et al. 2011; A. J. Drake et al. 2012; J. C. Mauerhan et al. 2013a; A. Pastorello et al. 2013; R. Margutti et al. 2014), the last of which was followed three years later by a presumably terminal explosion (although this interpretation is not conclusive; M. L. Graham et al. 2014). More recently, precursor activity has been detected in the SN IIn-P 2020pvb (N. Elias-Rosa et al. 2024), the normal SN II 2020tlf (W. V. Jacobson-Galán et al. 2022), the SN IIn 2021qqp (D. Hiramatsu et al. 2024), and the SN Ibn 2023fyq (S. J. Brennan et al. 2024; Y. Dong et al. 2024). These precursors were all detected in individual difference images, but systematic efforts are now underway to search for subthreshold emission preceding local CCSNe by coadding difference images (E. O. Ofek et al. 2014) or time-averaging photometry in bins leading up to the explosion (N. L. Strotjohann et al. 2021). High-cadence coverage of recent local events has also allowed us to place stringent limits on the luminosity of an optical precursor when an event is not detected either in single-visit difference imaging or through binning (e.g., 2023ixf (C. L. Ransome et al. 2024) and 2024ggi (M. Shrestha et al. 2024))[11].

In this nascent and rapidly evolving discovery space, several questions loom: is the pre-explosion mass loss of most terminal systems continuous or eruptive? What physical mechanism drives this emission, and what signatures does it imprint on the timescale and luminosity of the emission relative to the explosion? Is enhanced mass loss ubiquitous across core-collapse progenitors, and can it be used to identify the final stages of stellar evolution and predict the properties of a subsequent explosion?

Beginning its science operations for the 10-year Legacy Survey of Space and Time (LSST) in late 2025, the Vera C. Rubin Observatory (Ž. Ivezić et al. 2019) is expected to discover 1M SNe yr^{-1}, ∼50% of them CCSNe. Its deep ($r \sim 24$ and $i \sim 23.4$ in a single visit)[12] *ugrizY* photometry will enable broad studies of precursor demographics and volumetric rates. These data offer the potential to shift SN science from a *retroactive* discipline (the forensics of stellar death) to a *proactive* one (preparing for and witnessing the most local CCSNe in real time). A systematic investigation of the anticipated discoveries will better prepare the community for this shift.

In this work, we forecast the discovery rates of eruptive mass-loss episodes from hydrogen-rich CCSNe with the upcoming Rubin Observatory LSST. We separately consider the eruptions preceding SNe IIn and SNe IIP/IIL, and consider both theoretical models from previous studies and an observational model constructed from a single archetypal precursor event (that associated with SN 2020tlf). We consider these precursor episodes as standalone transient events without modeling an associated SN, due to the significant uncertainties surrounding their connection to stellar death.

We first explore the potential for characterizing precursor emission that passes LSST's detection trigger in individual differential photometry, which will be possible whether a subsequent explosion is observed or not. We call these "single-visit precursors," and assume the differential photometry is measured from deep templates with zero flux contamination. We also evaluate both the number and properties of precursors recovered by time-averaging multiple epochs of LSST photometry in fixed-width bins, as is common for retroactive searches.[13] We call these detected events "binned precursors." This latter technique will allow us to probe pre-explosion variability long

---

[10] A binary explanation is supported by strong evidence that the majority of massive stars form in binaries with separations low enough to undergo interaction during their lives (D. Vanbeveren et al. 1998; H. Sana et al. 2012).

[11] Precursor activity is likely in both of these events, with dramatic NIR variability revealed by Spitzer in the 2–3 yr preceding the former (C. D. Kilpatrick et al. 2023) and flash-ionization lines indicating the presence of CSM in the latter (W. V. Jacobson-Galán et al. 2024a)

[12] https://www.lsst.org/scientists/keynumbers

[13] Although we analyze differential photometry in this work, searching for emission in deep coadded images is also common.

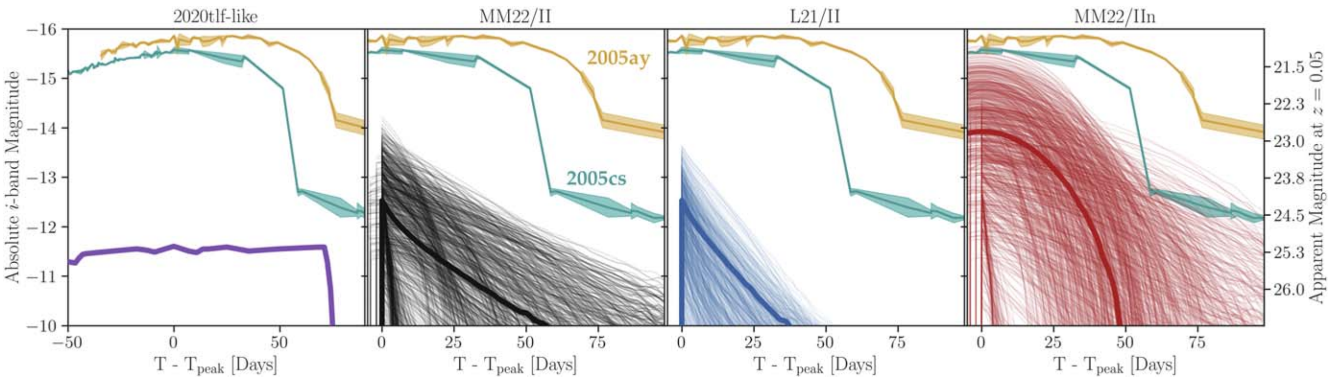

Figure 2. The *i*-band light curves for 1000 model SEDs (thin lines) and a single characteristic event (thick line) for the four CCSN precursor models considered. Precursors are color-coded by model type: 2020tlf-like (purple), MM22/II (black), L21/II (blue), and MM22/IIn (red). The *i*-band light curves for the extremely underluminous SNe IIP 2005cs (turquoise) and 2005ay (yellow) are shown for comparison. Phases for all light curves are shown relative to the *i*-band peak. Lower typical ejecta masses for the L21/II precursors relative to the MM22/II precursors lead to shorter-lived events. Priors on progenitor radius and additional SEDs above the RSG binding energy lead to higher typical luminosities for the MM22/IIn precursors.

before an associated SNe, in contrast with extant detections probing the final months preceding detonation.

Our paper is structured as follows. We describe our precursor models in Section 2.1, and the observational model used to generate synthetic LSST data in Section 2.3. In Section 3.1, we present our anticipated annual discovery rates in single-visit photometry. We expand this analysis to the first three years of LSST by binning differential photometry in Sections 3.2, and consider strategies to mitigate the impact of flux contamination in our reference photometry in Section 3.2.1. We then discuss the prospects for a local volume survey for eruptive precursors and their host galaxies in Section 3.3, and quantify the impact of our recovery rates on line-of-sight extinction in the case of a dust-enshrouded progenitor in Section 3.4. We summarize our results and conclude in Section 4. In all simulations, we adopt a cosmology of $\Omega_M = 0.3$, $\Omega_\Lambda = 0.7$, $w_0 = -1$, and $H_0 = 70\,\mathrm{km\,s^{-1}\,Mpc^{-1}}$.

2. Methods

2.1. Models for Eruptive Mass Loss

As the foundation of each of our theoretical models, we implement the eruptive precursor model described in T. Matsumoto & B. D. Metzger (2022a). This model calculates the light curve from hydrogen-rich ejecta with mass M_{ej} promptly launched by an eruption from the surface of a progenitor with radius R_*. The ejecta are assumed to expand homologously, and its velocity profile is characterized by density through the self-similar solution of A. Sakurai (1960), $v \propto \rho^{-\mu}$, where $\mu = 0.22$ (corresponding to the polytropic index of the envelope of $n = 3/2$). The ejecta are divided into multiple velocity shells and their thermal evolutions are independently solved. The bolometric luminosity is then calculated as the sum of the diffusion luminosity contributed by each shell. The spectrum is approximated by a blackbody with a temperature determined by the photosphere (the shell whose optical depth τ is unity). The model is parameterized by the minimum eruption velocity, v_{ej}, the total ejected mass, M_{ej}, the progenitor radius, R_*, mass, M_*, and polytropic index, n. This model does not encode a physical mechanism powering the emission, and is able to qualitatively reproduce the behavior of both short-lived (<50 days) and more long-lived (>100 days) precursors (T. Matsumoto & B. D. Metzger 2022a).

In this model, the peak luminosity of the observed emission is strongly correlated with the progenitor radius, as material becomes unbound more easily for progenitors with more tenuous envelopes. We assume an RSG progenitor to simulate the dominant contribution to the detected precursor population relative to more compact progenitors such as Blue Supergiants (BSGs). We fix $n = 3/2$ and $M_* = 10\,M_\odot$, and generate a model grid of 8000 spectral energy distributions (SEDs) spanning [1000, 15000] Å and [0, 200] d relative to eruption. For each SED, we sample R_* values in 20 log-uniform bins spanning $[100, 1000]\,R_\odot$, v_{ej} in 20 linear-uniform bins spanning $[0.1, 1] \times 10^3\,\mathrm{km\,s^{-1}}$, and M_{ej} in 20 linear-uniform bins spanning $[0.01, 1]\,M_\odot$. We refer to this model grid as "MM22/II," where the "II" designates a precursor model for SNe IIP/IIL (in contrast to precursors for SNe IIn, which we describe in additional detail below).[14]

An alternative eruption model developed by I. Linial et al. (2021) considers material shed from a polytrope and accelerated to the progenitor's escape velocity by a Sedov-like blast wave (L. I. Sedov 1946) launched from the stellar core (e.g., following a change in nuclear core burning). Through a series of hydrodynamical simulations, I. Linial et al. (2021) establishes a physically motivated range of ejecta masses associated with eruptive precursors to RSGs. This ejected mass range extends lower than the values considered in T. Matsumoto & B. D. Metzger (2022a), and is determined by the location at which the outward-propagating shock wave transitions from a slow to a fast shock. Because the energy deposition occurs deeper into the star than the T. Matsumoto & B. D. Metzger (2022a) model (where the material is launched directly at the surface), less mass is accelerated beyond the escape velocity to become unbound.

To explore a range of possible precursor events, we define a new model grid in which we sample ejecta masses within $M_{ej} \in [10^{-5}, 10^{-1}]\,M_\odot$, the range considered in I. Linial et al. (2021), and self-consistently update the minimum velocity of each precursor v_{ej} to the escape velocity of the progenitor. We refer to this model grid as "L21/II." We summarize the values of the sampled parameters in our MM22/II and L21/II model grids in Table 1.

---

[14] T. Matsumoto & B. D. Metzger (2022a) also explore pre-explosion mass loss due to enhanced winds, but the implementation of this model is beyond the scope of this work.

Table 1
The Parameters Sampled to Construct the Three Theoretical Models for Eruptive SN Precursors

Model	Parameter	Unit	Range/Value
MM22/II,IIn	R_*	$R_\odot$	[100, 1000]
	M_{ej}	$M_\odot$	[0.01, 1]
	v_{ej}	10^3 km s^{-1}	[0.1, 1]
L21/II	R_*	$R_\odot$	[100, 1000]
	M_{ej}	$M_\odot$	[10^{-5}, 0.1]
	v_{ej}		$v_{\rm esc}$

Note. The MM22/II and MM22/IIn models are constructed from the same SED grids, but with different selection cuts and priors on R_* (see text for details).

I. Linial et al. (2021) also require that the injected energy is lower than the binding energy of the system, or else no subsequent SN could occur. We apply a similar cut, and eliminate SEDs from our MM22/II grid for which the initial kinetic energy of the precursor exceeds the binding energy of the system (this condition holds for all L21/II SEDs, so none are removed). This leaves 3013 SEDs in the MM22/II grid. Imposing this cut forces the assumption for both models that a precursor is caused by energy injected at the center of the star—although, because the deposited energy at the stellar surface is always lower than the initial energy at the core due to radiative losses, our upper limit is a conservative one.

The L21/II model assumes the same $v \propto \rho^{-\mu}$ ejecta velocity profile as the MM22/II model. As in T. Matsumoto & B. D. Metzger (2022a), the L21/II SEDs are generated by summing the luminosity contributions of a set of discrete velocity shells in time, solving for the photospheric radius and temperature of the system, and calculating the wavelength-dependent flux of the precursor assuming blackbody emission. For the lowest-mass and highest-velocity models in our grid, this results in an early shock-breakout-like peak as the ionized hydrogen from the highest-velocity shell recombines. Because this phenomenon is specific to the assumed mass profile of the ejecta, we manually remove the early peak from each light curve in both the L21/II and MM22/II grids so as not to positively bias the detection statistics.

Precursor activity has been discovered in only a single normal SN II, 2020tlf (W. V. Jacobson-Galán et al. 2022). Deep PS1 photometry showed enhanced, persistent emission for 130 days prior to explosion. Although the general timescale of this emission can be reproduced by the MM/II model, the early peak of the model leads to discovery statistics inconsistent with its observed counterpart. To further improve our predictions, we translate the reported bolometric luminosities of the SN 2020tlf precursor in W. V. Jacobson-Galán et al. (2022) into a third SED model, assuming blackbody emission. We call this precursor model "2020tlf-like."

Significantly more precursors have been discovered preceding SNe IIn (N. L. Strotjohann et al. 2021), in some cases reaching peak luminosities comparable to the lowest-luminosity CCSNe (e.g., the SNe IIP 2005cs and 2005ay, which exhibited plateaus with $M_V > -16$; D. Y. Tsvetkov et al. 2006). Although the physical mechanism underlying these precursors is unknown, the most luminous SN IIn precursors suggest energies likely to unbind an RSG if deposited at the core. Recently, D. Tsuna et al. (2024a) proposed a model by which interaction from a compact companion can inject additional energy into the outer envelope of an RSG, allowing precursors to exceed this limit. We further develop a grid of SN IIn precursor SEDs by considering the full 8000 T. Matsumoto & B. D. Metzger (2022a) SEDs (before imposing a precursor energy cut) and imposing a prior on R_* from binary stellar models in MESA (discussed in the following section). This forms our fourth precursor model grid, which we call "MM22/IIn."

Since the luminosities of a precursor depend in part on the radius of the progenitor launching them, we employ a prior on R_* such that our models reflect a physically motivated underlying stellar population. We discuss these priors in the following section.

2.2. Constructing Priors for the Progenitor Radii of Simulated Precursors

We impose empirical priors on the distribution of CCSN progenitor radii with a separate suite of single and binary stellar evolution models (A. Gilkis & E. Laplace et al. 2024, in preparation) using version 15140 of the Modules for Experiments in Stellar Astrophysics (MESA; B. Paxton et al. 2011, 2013, 2015, 2018, 2019) code.[15] We assume a mixing length parameter of $\alpha_M\mathrm{LT} = 2$ for all simulations. In superadiabatic regions, we employ the MLT++ method (B. Paxton et al. 2013) at late evolutionary stages (after carbon depletion) for models with $\log_{10}(T_{\rm eff}/\mathrm{K}) < 4.3$, or $\log_{10}(T_{\rm eff}/\mathrm{K}) < 5.025$ and $\log_{10}(L/L_\odot) < 5.65$ at core carbon depletion. In all other models, the `use_superad_reduction` option is used.

Simulations were run for three different assumed metallicities: that of the SMC ($Z = 0.00224$), the LMC ($Z = 0.0056$), and the Milky Way ($Z = 0.014$). For the binary simulations, the initial conditions were 27 initial primary masses between 4 and 99 $M_\odot$, 3 mass ratios (0.25, 0.55, and 0.85), and 14 initial orbital periods evenly distributed in log-space between 2 and 2223 days. For single stars, 92 initial masses were used, including those of the primaries in binaries. The explosibility in simulations that reached iron core collapse was determined following B. Muller et al. (2016), and in simulations that reached the end of core carbon burning but not iron core collapse, an explosion was assumed if the CO-core mass was above the Chandrasekhar mass and below 9 $M_\odot$. In total, 1534 simulations were considered to represent SN progenitors: 109 single stars, 1031 primaries in binaries, and 394 merged stars resulting from coalescence during common envelope evolution following unstable mass transfer. Models with hydrogen mass greater than 0.033 $M_\odot$ at the end of the simulation were taken to represent a population of SN II progenitors (S. Hachinger et al. 2012; A. Gilkis & I. Arcavi 2022).

We find negligible differences in the radius distributions of the three metallicities, and select the Milky Way model set as our CCSN progenitor radius distribution. We use the `stats` module in `Scipy` to compute a kernel density estimate (KDE) of R_*, and sample our KDE with 301 log-uniform bins in the range $\log(R_*/R_\odot) \epsilon$ [2, 4]. In our subsequent LSST simulations, we reweight the flat probability density function of our precursor SEDs (for both MM22/II and L21/II) by this distribution. For our MM22/IIn models, we adopt the distribution of progenitor radii of all stars in binary systems as our prior on R_*. To prevent adding an extra dimension to our precursor model grids, we do not weight our SEDs by the distribution of progenitor masses from these simulations; our detection statistics are only weakly dependent on M_*.

---

[15] All MESA runs can be downloaded via Zenodo doi:10.5281/zenodo.14047988.

We plot the priors on progenitor radii for our IIP/IIL and IIn precursors in Figure 1. We find a clear overdensity near $R_* \sim 10^3\, R_\odot$, and a slight overdensity at higher radii for binary CCSN progenitors relative to the full population. For comparison, we show the reported progenitor radii for the Type II SN 2004A, SN 2009ib, SN 2017eaw, SN 2017gmr (J. A. Goldberg & L. Bildsten 2020), and SN 2024ggi (D. Xiang et al. 2024). Despite the small number of events, we find broad agreement with the SN II progenitor estimates from literature. We caution that our MESA models have assumed hydrostatic equilibrium, and a violation of this assumption in the case of, e.g., radial pulsations will lead to variations in the adopted radius distribution.

We also show the radius estimates for a sample of Galactic LBVs from L. Mahy et al. (2022) in Figure 1. The majority of estimates fall toward the low-density tail of the binary system distribution, inconsistent with the direct detection of LBV progenitors in the case of the SNe IIn SN 2005gl (A. Gal-Yam & D. C. Leonard 2009) and SN 2009ip (N. Smith et al. 2010; R. J. Foley et al. 2011). We caution that, at the luminosities of these LBV-like IIn progenitors, our MESA simulations predict direct collapse into a black hole with no associated SN. Late-stage eruptive mass loss may alter the core structure of these progenitors, altering their explosibility and our subsequent progenitor radius priors (e.g., S. E. Woosley 2019; E. Laplace et al. 2021). Nonetheless, as we discuss in subsequent sections, the resulting model grid is able to reasonably reproduce the properties of observed SN IIn precursors without excessive fine-tuning of the sampled precursor energies. We note that, for a fixed progenitor mass, a decrease in progenitor radius will lead to a less luminous precursor (Figure 4 from T. Matsumoto & B. D. Metzger 2022a), leading to greater inconsistencies between our IIn precursor simulations and those reported in N. L. Strotjohann et al. (2021). This inconsistency suggests that additional interaction (of a binary progenitor or between multiple shells/clumps of surrounding CSM) contributes to the observed emission of precursors, as will be discussed later.

We plot high-cadence, noise-free light curves in the LSST *i* band for our four precursor scenarios in Figure 2. We show 1000 realizations of each model with low opacity, and a single representative event as a solid line. As expected, the *i*-band brightness of the 2020tlf-like model stays roughly constant for longer than each of the other models. The lower ejecta masses of the L21/II model relative to the MM22/II model manifest in a population of shorter-lived events. The typical brightness of events from the MM22/IIn model grid generally exceeds those of the other three models, and the longest-lived events exceed 75 days. For comparison, we also show *i*-band photometry for the low-luminosity SNe IIP 2005ay and 2005cs retrieved from the Open Supernova Catalog API.[16]

2.3. A Forward Model for LSST Observations

We use the `SNANA` simulation code (R. Kessler et al. 2009) as a forward model for our synthetic LSST observations. The LSST DESC collaboration[17] has produced cadences associated with existing and upcoming sky surveys that can be used by the simulation (OpSim; R. Biswas et al. 2020). Starting from a grid of rest-frame SEDs for a transient model, the `SNANA` code draws an SED (its selection can be weighted, as is done here for progenitor radius), places the transient at a random sky position, reddens it according to the Galactic extinction along the line of sight, and selects a random redshift based on a chosen volumetric rate (our adopted volumetric rates will be discussed in detail below). Synthetic magnitudes are computed using filter transmission curves and a cadence associated with a proposed survey strategy. An observed flux and its associated uncertainty are determined for each synthetic magnitude using the OpSim-generated zero point, sky noise, and PSF. Detections from the DESC Difference Imaging Analysis pipeline[18] are based on a computed curve that tracks efficiency versus the signal-to-noise ratio (S/N) for LSST (R. Kessler et al. 2019; B. O. Sánchez et al. 2022), obtained through the injection of point sources in synthetic LSST images from the DC2 sky simulations (LSST Dark Energy Science Collaboration et al. 2021). To minimize spurious detections from Poisson fluctuations, we impose a trigger requirement of two detections separated by more than 30 minutes for discovery.

We adopt the latest baseline v3.4 LSST survey strategy in our simulations,[19] which was released in 2024 May and includes the primary Wide–Fast–Deep (WFD) survey, the subsurvey of five deep drilling fields (DDF), a rolling cadence, and a fraction of observational triplets to increase the median cadence of observations in a single photometric filter. Additional details on this strategy can be found in the Rubin Observatory's Survey Cadence Optimizations Committee recommendations document.[20] While the exact survey strategy adopted by the Rubin Observatory is actively evolving, variations at this stage are expected to be minor and are unlikely to substantially alter the results reported here.

We assume that all IIP/IIL and IIn SNe are preceded by an eruptive precursor, and adopt the same volumetric rates for their precursors. For our IIP/IIL precursor models (2020tlf-like, MM22/II, and L21/II), we multiply the volumetric CCSN rate from L.-G. Strolger et al. (2015) by 0.87, following the volumetric fraction estimated from the LOSS sample in I. Shivvers et al. (2017). For our MM22/IIn model, we multiply the rate by 0.05 (I. Shivvers et al. 2017; C. Cold & J. Hjorth 2023).

We caution that these rates are likely an overestimate, given the results of E. O. Ofek et al. (2014), N. L. Strotjohann et al. (2021), and A. Reguitti et al. (2024), but we emphasize that serendipitous precursor discoveries among both SNe IIn and the SN II 2020tlf have been driven by targeted searches preceding nearby explosions. Given the limited depth and baseline coverage of current wide-field surveys (ZTF was commissioned in 2018 and is multiple magnitudes shallower than the Rubin Observatory in a single pointing), LSST data can be used to probe fainter, earlier precursors than have been found to date.[21] A multi-year archival search among extant wide-field photometric surveys will shed additional light on relative rates, but the tightest constraints will come from the Rubin Observatory itself.

For each precursor grid, we run two simulations. In the first, we simulate the number of precursors recovered in single-epoch photometry spanning the first year of LSST operations (MJD 60796 to 61161). We impose an additional selection cut

---

[16] https://github.com/astrocatalogs/OACAPI

[17] https://lsstdesc.org/

[18] https://github.com/LSSTDESC/dia_pipe

[19] https://community.lsst.org/t/release-of-v3-4-simulations/8548

[20] https://pstn-055.lsst.io/

[21] A. Reguitti et al. (2024) caution that their discovery of precursor activity in $\sim$30% of SNe IIn is an underestimate of the intrinsic rate driven by observational biases.

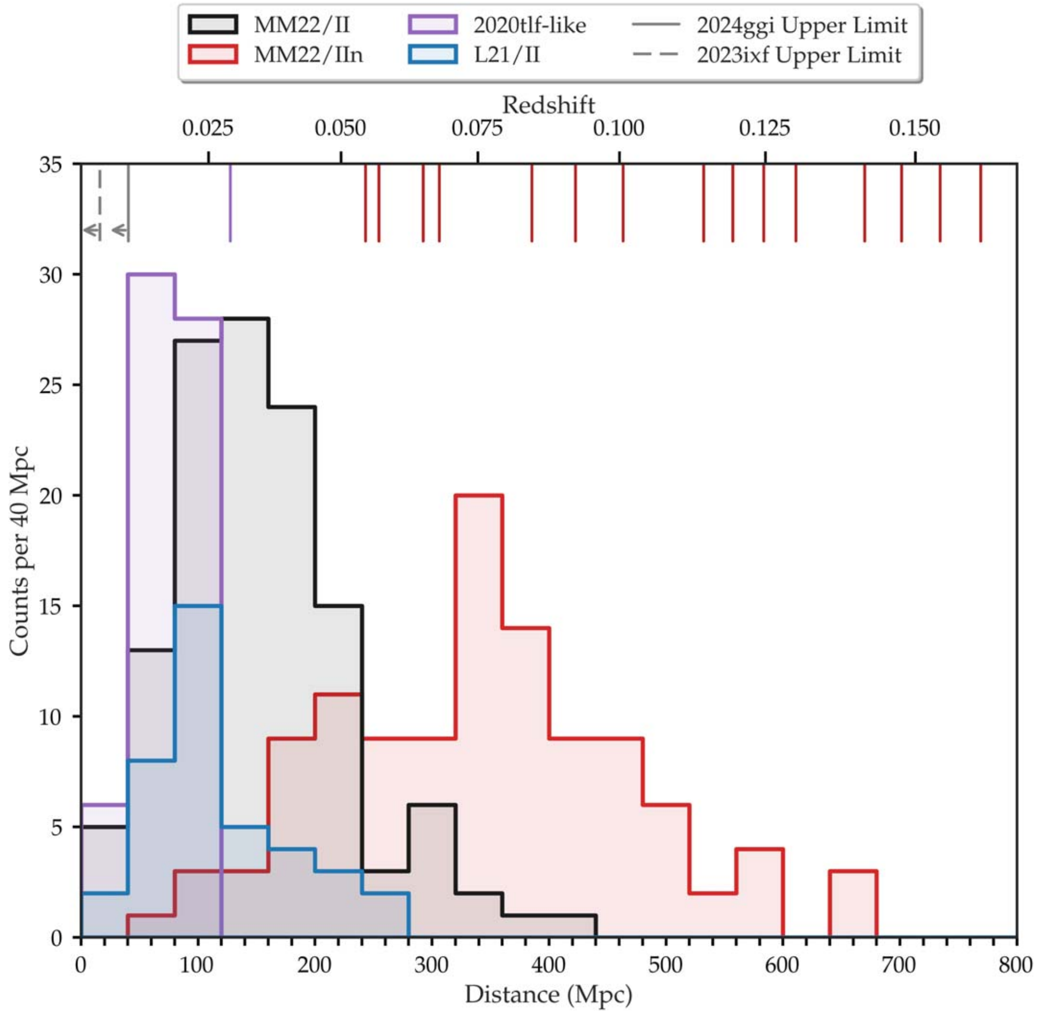

Figure 3. Histogram over distance for the single-visit precursor events passing our two-detection trigger in one year of LSST. The vertical lines at the top reflect the distances at which observed precursors to 2020tlf (shown in purple) and SNe IIn (red) from N. L. Strotjohann et al. (2021) reach the single-visit limiting magnitude of LSST in *r*. Gray vertical lines indicate the upper limits of precursor emission in 2023ixf (C. L. Ransome et al. 2024) and 2024ggi (M. Shrestha et al. 2024).

beyond the trigger criterion, and require at least two detections with a signal-to-noise ratio $\geqslant$5 in any bands. In the second simulation, we exclude the detection trigger and our selection cut and write out all events occurring within the observing footprint of the simulated survey. We expand our simulation to the first three years of LSST operations in the second simulation (spanning MJD 60796 to 61526) to mitigate variations due to Poisson statistics, which become relevant when examining binned events discovered in DDF fields.

3. Results

3.1. Annual Discovery Rates from Single-visit Observations

We first consider the events passing our detection trigger in single-epoch differential photometry (our "single-visit precursors"). We present histograms for the detected event distances of our four models in Figure 3. We define the median distance $\tilde{d}$ and the 90th percentile of detection distances d_{90} for each model. Due to their low luminosity, 2020tlf-like events are only detected to $\tilde{d} \approx 74$ Mpc and $d_{90} \approx 108$ Mpc. Because the distribution for our L21/II models extends toward lower-mass precursors, we observe systematically lower distances for the detected population relative to the T. Matsumoto & B. D. Metzger (2022a) grid: we detect L21/II events with $\tilde{d} \approx 110$ Mpc and $d_{90} \approx 205$ Mpc, compared to MM22/II events with $\tilde{d} \approx 143$ Mpc and $d_{90} \approx 241$ Mpc. The luminous MM22/IIn precursors are detected to significantly greater distances, with over twice the median distance ($\tilde{d} \approx 340$ Mpc) and over twice the d_{90} distance of the second-highest model ($d_{90} = 497$ Mpc). We summarize these metrics and the total number of detections for all single-visit precursors in Table 2.

For comparison, we also show the maximal LSST detection distances of the SN 2020tlf precursor from W. V. Jacobson-Galán et al. (2022) and observed SN IIn precursors from N. L. Strotjohann et al. (2021) (using the anticipated LSST limiting magnitude) as vertical lines in Figure 3. Overall, we find good agreement between our simulated detection distances and the observed events. The observed SN IIn precursors extend toward the higher end of our predicted distribution, but this is due to the greater abundance of longer-lived events that can be recovered through binning (as is done in N. L. Strotjohann et al. 2021). We also show the reported upper limits for emission preceding the nearby Type II SN 2024ggi and SN 2023ixf from M. Shrestha et al. (2024) and C. L. Ransome et al. (2024), respectively. Neither event showed optical signatures of precursor activity, despite their close proximity; we will return to these events in Section 3.4.

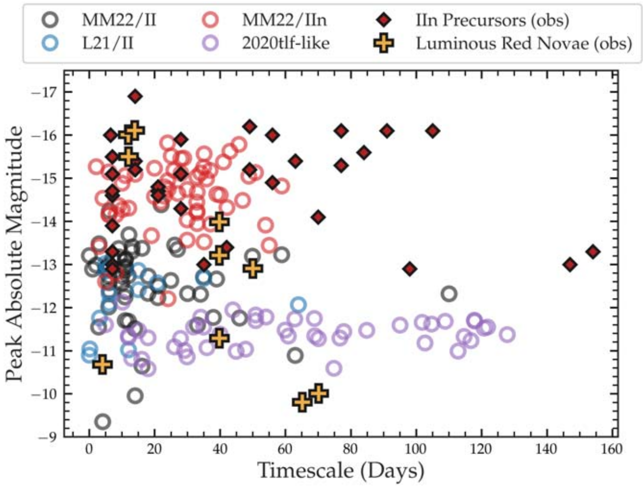

Figure 4. Brightness vs. observed timescale for the single-visit precursors passing the detection trigger, where the timescale is defined as the number of days from first to last 5σ detection in any band. Models are listed in the legend. Also shown are the brightnesses and timescales for observed SN IIn precursors from N. L. Strotjohann et al. (2021), as well as those of LRNe reported in M. M. Kasliwal (2013).

Table 2
Median Distance, 90th-percentile Distance, and Total Number of Single-visit Precursors Detected in One Year of LSST

Model	$\tilde{d}$ (Mpc)	d_{90} (Mpc)	N_{tot}
MM22/II	143	241	125
L21/II	110	205	39
2020tlf-like	74	108	64
MM22/IIn	341	497	112

Next, we investigate the properties of the discovered events. We plot the peak absolute brightness in any band for the single-visit precursors as a function of the observed timescale, which we have estimated as the number of days from first to last detection in any band. We caution that this observational definition does not directly correspond to the intrinsic timescale of an event, in particular for events poorly characterized at higher redshifts. We present the results in Figure 4, and compare our simulations to the properties of the reported IIn precursors from N. L. Strotjohann et al. (2021). We also overplot a sample of luminous red novae (LRNe) from M. M. Kasliwal (2013). These transients are believed to be powered by hydrogen recombination following the ejection of a common envelope or merger of a binary stellar system (A. Pastorello et al. 2019), and their similarity to IIn precursors has been discussed extensively in the literature (the T. Matsumoto & B. D. Metzger 2022a model we employ has also been used to model LRNe; see T. Matsumoto & B. D. Metzger 2022b).

The brightness distribution of synthetic and observed IIn precursors is comparable, but we are unable to reproduce the subpopulation of longer-lived (>50 days) IIn precursors. We note that multiple precursor events spanning ∼100 days have been reported for the SNe IIn in N. L. Strotjohann et al. (2021). Because these long-lived events will be easier for LSST to detect in both single-visit and binned searches, our subsequent annual rates for SN IIn precursors can be taken as a conservative estimate.

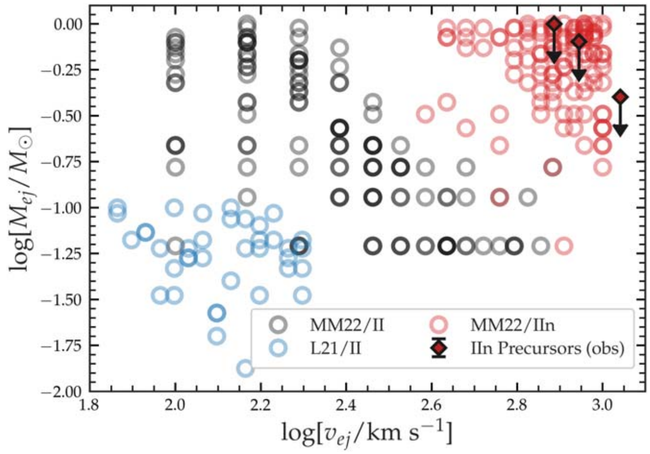

Figure 5. Ejecta masses as a function of the minimum ejecta velocities for the single-visit precursors passing the detection trigger. Precursor models are listed in the legend. We also show the properties of well-constrained IIn precursors detected in N. L. Strotjohann et al. (2021): their estimated CSM velocities from narrow line profiles in early SN spectra, and upper limits to the inferred ejecta mass from SN rise times.

We observe significant scatter in the estimated timescale for 2020tlf-like events due to the flat, long-lived emission, which can sit at the LSST detection limit and be marginally detected above the noise in only a few observations. As expected, the observed population of LRNe spans the full parameter space of our precursor models. This makes them a primary contaminant of upcoming precursor searches.

Next, we consider the distribution of physical parameters for single-visit MM22/II, MM22/IIn, and L21/II precursors. We plot M_{ej} versus v_{ej} for detected events in Figure 5, and superimpose the well-constrained velocities and ejecta mass limits reported by N. L. Strotjohann et al. (2021). The CSM velocities in this work have been estimated from shock-ionization line profiles, and the mass limits are inferred from the maximum allowable diffusion time consistent with the timescale of the subsequent SN rise. Again, we find good agreement between detected and simulated IIn precursors, although we caution that the literature values are order-of-magnitude estimates. We find minimal overlap between parameter properties between models, with L21/II precursors occupying the lowest velocities and ejecta masses.

In Figure 6, we compare the total number of detections for each single-visit precursor versus the number of days between first and last detection. Events in the top right corner of this phase space are ideal for photometric and spectroscopic follow-up, while follow-up will not be possible for the events in the bottom left. Again, we find a strong dependency on model type, with 2020tlf-like precursors being ideal follow-up targets, due to their longer timescales, followed closely by MM22/IIn precursors, due to their high relative luminosities.

3.2. Annual Discovery Rates from Binned Photometry

Discovery from a two-detection trigger may be possible for the brightest tail of the precursor luminosity distribution, but the majority of *observed* precursors have been discovered through stacking of archival photometry *a posteriori* once an SN is found. We investigate this possibility by excluding all LSST detection triggers from our observing model and saving the differential photometry for all events of each model simulated within $z < 0.3$ and across the first three years of LSST.

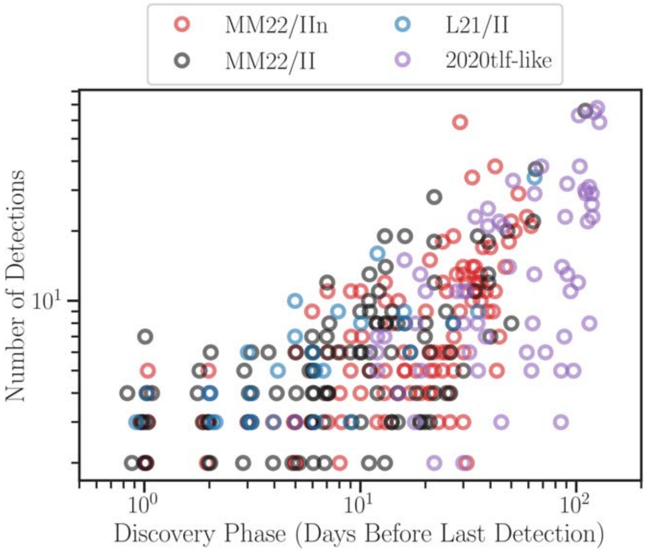

Figure 6. Total number of photometric detections vs. the time difference between first and last detection for single-visit precursors. Events at the top right are ideal for spectroscopic follow-up, while data for events at the bottom right are unlikely to be scientifically valuable. Trends in this space are reflective of the luminosity–timescale relation of each precursor model (Figure 4).

For each event, we bin the differential photometry separately in each LSST filter using a fixed bin size N in days. We adopt a similar detection criterion for our binned photometry as for the unbinned case, and require at least one $S/N \geqslant 5$ binned detection. We consider four bin sizes: $N = 1$, 20, 50, and 100 days. Because the typical single-filter cadence of LSST in Wide–Fast–Deep mode is ∼18 days, bin sizes less than 20 days are unlikely to consistently capture more than a single observation. Further, the vast majority of our precursors do not last longer than 50–75 days; using a wider bin would average out any potential detections with the background.

We present the three-year recovery statistics for our four classes in the WFD and DDF surveys across all bin widths in Figure 7, and overplot the single-visit detections described in the previous section. We find a ∼70% increase in the median detection distance in the three-year WFD photometry relative to single-visit across all models: up to 431 Mpc for the MM22/IIn precursor, 206 Mpc for the MM22/II precursor, 162 Mpc for the L21/II precursor, and 94 Mpc for 2020tlf-like precursors. The WFD distributions all feature a substantial positive skew, where faint precursors are marginally detected above the background. We also show example precursors with binned detections above 5σ for each bin width in the Appendix.

As expected, the median detection distance is also higher in the DDF fields than in WFD, as a result of the higher single-band cadence. In all SN II models (MM22/II, L21/II, and 2020tlf-like), we nearly double our median recovery distance relative to WFD. These longer-lived, more abundant precursors relative to the MM22/IIn model are significantly aided by the increased DDF cadence. The median distance for recovered MM22/IIn precursors increases by a smaller fraction, from 432 to 637 Mpc. This is a consequence of the relative luminosity of these events and the lower assumed volumetric rate (such that a larger fraction of the intrinsic population is detected with the baseline WFD cadence than the SN II precursors).

Finally, we present the peak absolute brightness as a function of distance for all single-visit and binned precursors in Figure 8, and compare these to the 5σ single-visit r-band detection limit of LSST and ZTF. We find that the vast majority of detections for all precursor models surpass the ZTF r-band single-visit 5σ depth of ∼20.8 (F. J. Masci et al. 2019), reflecting the necessity of the Rubin Observatory to characterize dim transient populations such as the ones considered here. We also find that the events discovered by binning will have very few statistically significant detections for characterization, and they may only be scientifically valuable to constrain demographics (unless timescales are inferred by comparing multiple binning approaches, as we discuss in Section 3.2.1).

We can broadly compare our recovery statistics in Figure 8 to previously detected precursors. Given the observational biases associated with targeted binned searches, we limit our comparison to precursors recovered in our single-visit simulation. N. L. Strotjohann et al. (2021) report (their Figure 2) that precursor emission was securely detected at the 5σ level preceding 14 SN IIn in single-visit (unbinned) ZTF pointings, versus none in our one-year simulation. In 10 of these SNe, the brightest detected precursor event had a *median* flux of $M < -15$ in either ZTF-g or ZTF-r, brighter than the vast majority of MM22/IIn events. Earlier simulations have been similarly unable to reproduce this high-luminosity tail of observed SNe IIn (e.g., J. H. Shiode & E. Quataert 2014).

Given the existence of bright, long-duration SN IIn precursors not captured by our simulation framework, we have compared our annual single-visit detection rates with those from a simpler IIn precursor model consisting of persistent emission for ∼100 days and peaking at $M \approx -16$. The relative rarity of these brighter events among the sample analyzed by N. L. Strotjohann et al. (2021) (associated with ∼1% of all SNe IIn, and ∼5% of long-lasting precursors <90d from explosion; see Figures 7 and 8 of N. L. Strotjohann et al. 2021) corresponds to a detection rate of ∼10 yr^{-1} with the LSST, subdominant to our reported IIn rate. However, we caution that these statistics are highly sensitive to the assumed proportion of this bright subpopulation; a relative fraction of 2% (within 1σ of the fraction reported by N. L. Strotjohann et al. 2021) leads instead to a detection rate of ∼30 yr^{-1}, with multiple now detected above the ZTF detection limit.

In 11 of the 14 SNe with single-visit precursor detections, the brightest detected precursor occurred in the final month preceding detonation. CSM velocities far above the values considered here ($v_{ej} > 10^3$ km s^{-1}) could increase the luminosity of the observed precursor, but would be inconsistent with values inferred from spectroscopy. Kinetic energy from the interaction between multiple CSM shells ejected prior to the explosion can contribute additional luminosity to an observed precursor, and is suggested by the detection of multiple precursor events preceding several of the SNe IIn reported in N. L. Strotjohann et al. (2021). Early eruptions may also alter the density structure of a progenitor envelope, decreasing the photon diffusion time and increasing both the luminosity and duration of subsequent precursor emission (N. Kuriyama & T. Shigeyama 2021). Modeling the long-term response of the progenitor system to these eruptions, as well as the interaction of the CSM from distinct outbursts, may be necessary to reproduce the full diversity of SN IIn precursors.

Next, we consider unbinned detections of SN IIP/IIL precursors. Each of our SN II models (MM22/II, L21/II, and 2020tlf-like) predict precursor emission detectable in unbinned photometry above the 5σ magnitude limit of ZTF, yet none have been discovered to date. We caution that the timescale and

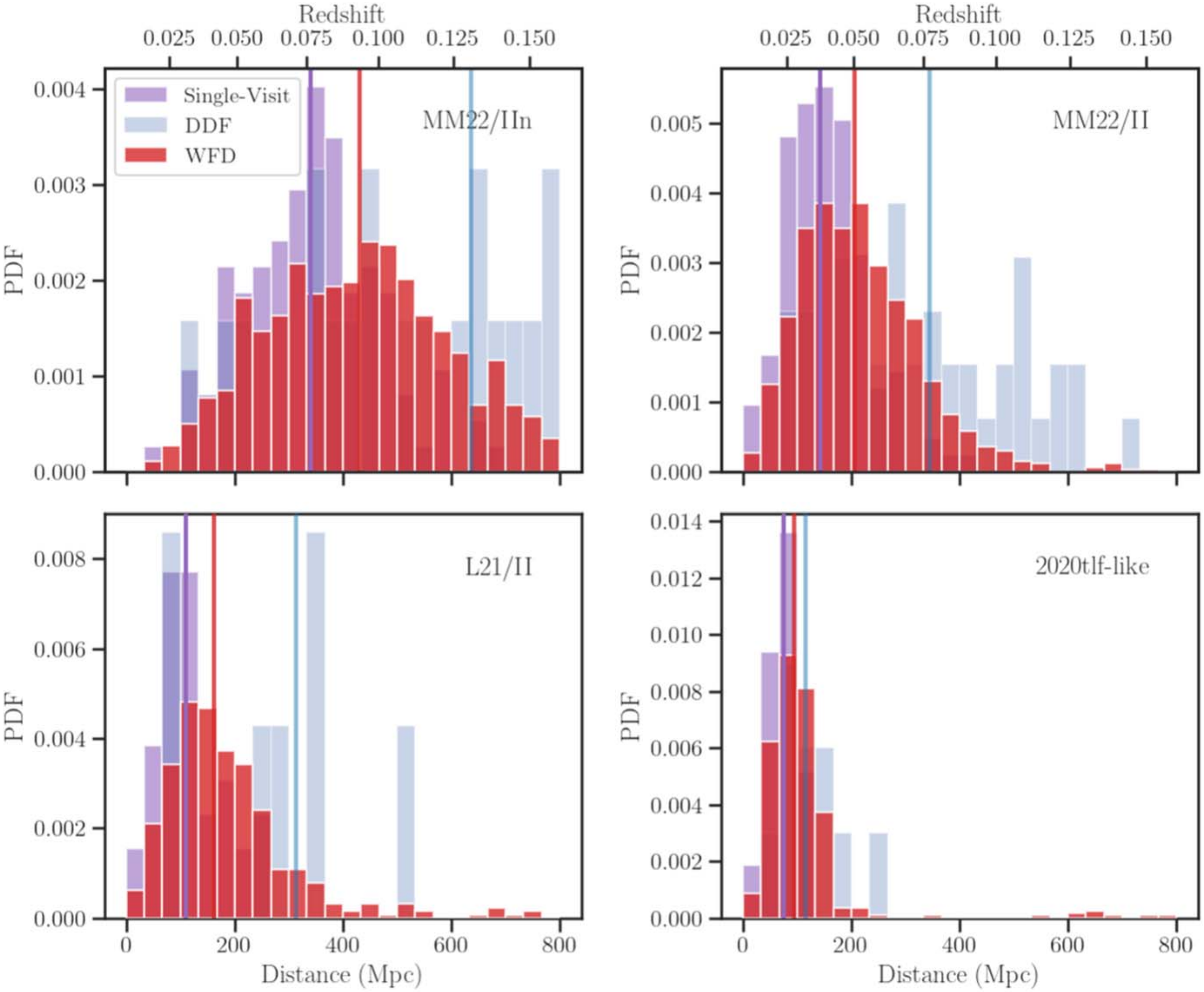

Figure 7. Distances of precursors detected in LSST data in the idealized binning case at any bin width during the first three years of the primary WFD survey (red) and the DDF survey (blue). For comparison, we also show the distances of precursors from our 1 yr single-visit study described in Section 3.1 (purple). The median of each distribution is shown as a solid line.

SED of potential SN IIP/IIL precursors is highly uncertain, informed only by the observational constraints provided by SN 2020tlf (and the single-epoch luminosity and blackbody properties of this precursor are not well-constrained). A decrease in the inferred blackbody temperature of 2020tlf-like events of a factor of two pushes the peak of the emission into the infrared and beyond the reach of ZTF (though it may still be detected in LSST-*y*). Furthermore, the persistent emission observed in the 2020tlf precursor may be more consistent with an enhanced wind rather than eruptive mass loss (W. V. Jacobson-Galán et al. 2022; T. Matsumoto & B. D. Metzger 2022a). Finally, as we discuss in Section 3.4, extinction from dust surrounding the SN II progenitor may render these dimmer precursors undetectable at optical wavelengths.

3.2.1. Strategies for Binning Pre-explosion Photometry in the Case of Multiple Precursors

By default, our simulations have assumed that the templates used to calculate differential photometry contain zero flux. In practice, the selection of a baseline flux level for binning studies is a nontrivial task. Sky noise leads to stochastic variations in flux, host-galaxy light can be substantial for these local events, and a reference flux baseline chosen across some pre-explosion window could be contaminated by marginal emission from the current or a separate undetected precursor event.

To explore strategies to mitigate template contamination by precursor emission, we use the SEDs in Figure 2 to calculate the average flux contribution in each LSST passband from each of the precursor models. We consider three strategies for baseline flux estimation:

I. Baseline Averaging, 50 days. In the first strategy, we average the flux contribution from the first 50 days of precursor emission, mimicking the pessimistic case in which a precursor is fully captured in the coadded template and the template spans the approximate timescale of precursor emission. We adjust the raw differential fluxes from our three-year simulation according to these new model-specific baselines and repeat our experiment, binning the resulting photometry in 1, 20, 50, and 100 day bins.

II. Baseline Averaging, 500 days. In the second case, we average the flux contribution across 500 days, starting at the

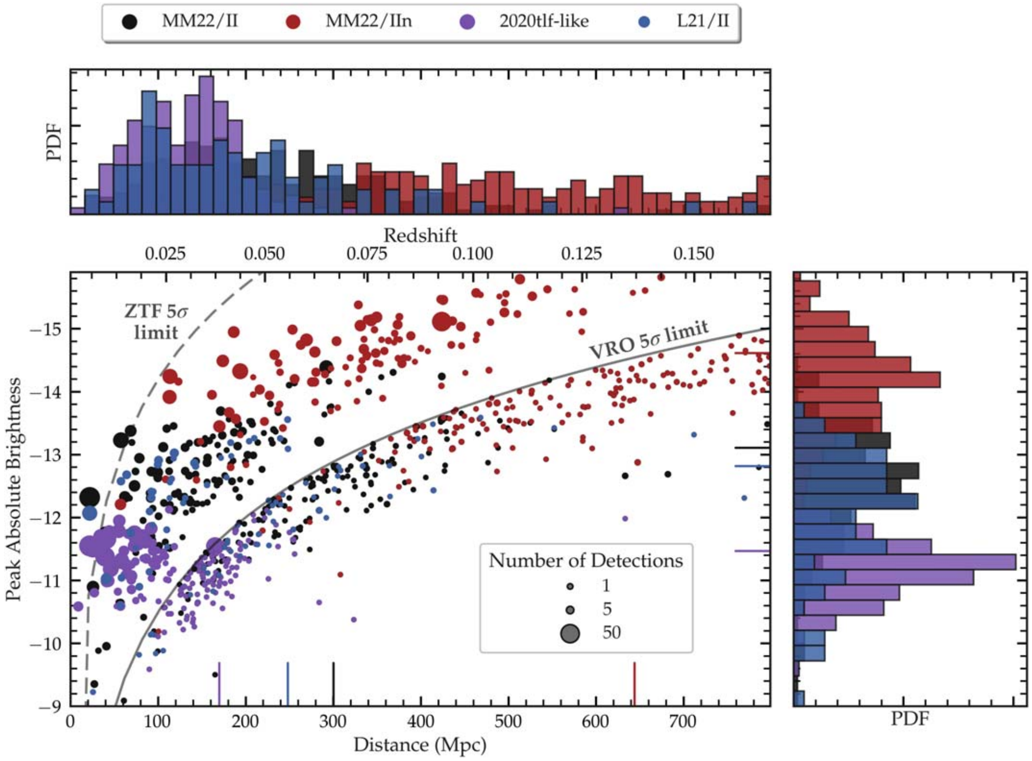

Figure 8. All single-visit and binned CCSN precursors from one year of synthetic LSST observations. Color corresponds to the precursor model assumed (given in legend), and point size corresponds to the total number of 5σ detections for that precursor. The dashed gray line corresponds to the r-band single-visit 5σ detection limit of the Zwicky Transient Facility, and the solid gray line corresponds to the r-band single-visit 5σ detection limit of the Rubin Observatory. Binned detections are only shown beyond the single-visit VRO detection limit for clarity. Colored lines at bottom and right give the upper 75th percentile for distance and peak brightness for each model type.

eruption time of each precursor, in the hopes of averaging out the added flux in the contaminated template.

III. Iterative Median. In the third case, we employ a similar iterative median strategy to the one introduced in N. L. Strotjohann et al. (2021) to find SN IIn precursors. For each LSST band, we choose a 500 day window starting from eruption time. We calculate the median raw flux across all observations, remove the observation with flux farthest from the baseline (not considering uncertainties), and recalculate the median flux. We repeat this process until 20% of the data are left, and select the final median flux as our baseline value in each passband. We then average the contribution across all light curves for each model at a fixed distance. During our binning experiments, we calculate this baseline flux contribution at the distance of our candidate precursor.

We report the total number of events recovered, and the 70th percentile of their detection distance d_{75}, as a function of bin width for each of our three cases (50 and 500 day baseline averaging, and iterative median) compared to our "ideal" uncontaminated baseline, in Figure 9.

The d_{75} distance of recovered precursors is fully determined by the chosen model and bin width, and is not impacted by the baseline strategy adopted. We find the most significant absolute decrease in detection distance across bin widths with the L21/II model, from 240 Mpc with 1 day bins to 200 Mpc with 100 day bins. The MM22/IIn precursors are recovered to comparable distances with every bin width, a result of their high intrinsic luminosities and low volumetric rates relative to the other models.

In the ideal (zero template flux) case, we find an increase in the number of detected events with 20 day binning across all models. With the MM22/II and L21/II models, we observe a decrease in detected events with 50 and 100 day bins, and a similar reduction with 100 day binning for our MM22/IIn model. In contrast, a monotonic increase in the number of detected 2020tlf-like events can be seen when increasing the bin width from 1 to 100 days. These differences are reflective of the different phenomenology of each event, and may be useful for broadly characterizing precursor timescales even if individual events are not well-constrained.

When contaminated flux for the 2020tlf-like precursor is averaged across a 50 day window, we lose ~50 precursors at every bin width considered. We recover our full detected population equally by extending our averaging window to 500 days or employing the iterative median strategy. We conclude that our recovery statistics are not significantly impacted by contaminated templates, except in the case of 2020tlf-like precursors. We note that, if the flux baseline is systematically increased, a precursor may still be detectable by looking for statistically significant flux *decreases*. These transient events will be flagged in the LSST alert pipeline.

To investigate the impact of Poisson fluctuations on our recovery statistics, we dim the SED of our 2020tlf-like model by 20 magnitudes and run the same binning experiment on all raw flux values at the location of each transient. In our flux-free template, we find no 5σ detections at any bin width, indicating that our precursor estimates are precise. A caveat exists for the 50 day iterative binning technique where the template is contaminated by precursor flux: the technique led to the spurious "identification" of 2–5 events at all bin lengths. We therefore caution that this approach, while able to mitigate the

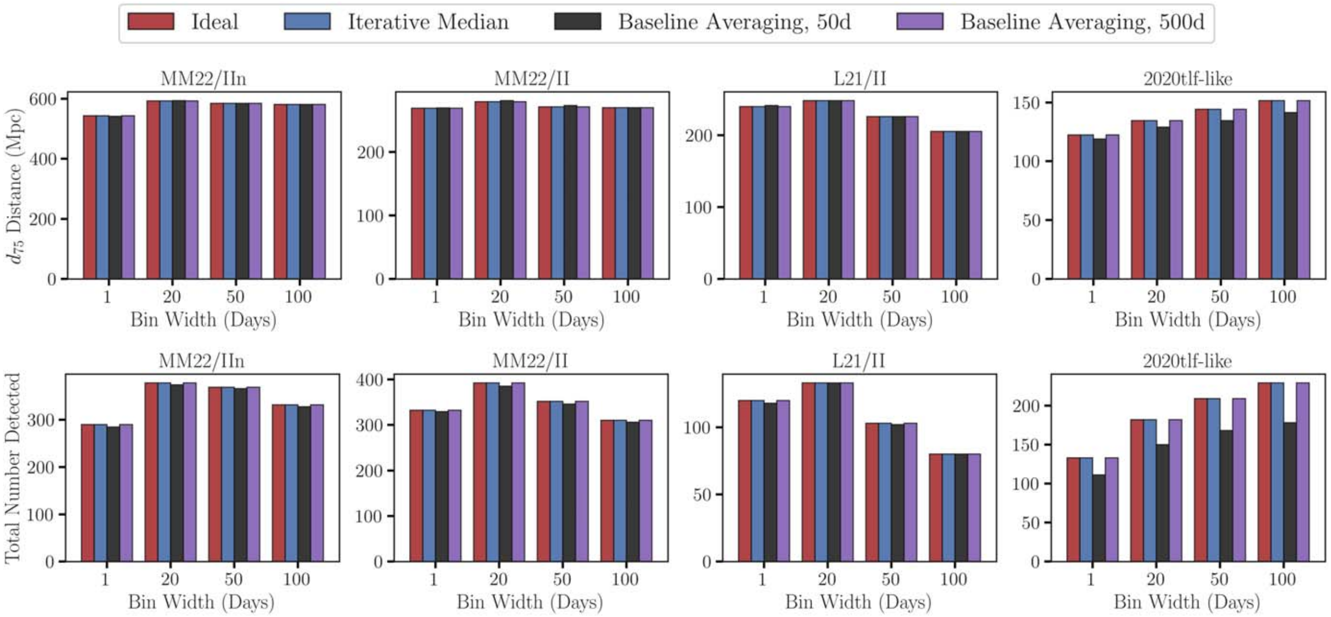

Figure 9. Maximum distance (top) and total number (bottom) of detected precursors in three years of LSST operations as a function of bin width for the four models in this work. Binning with greater than 20 day bins improves the recovery statistics for the long-lived 2020tlf-like precursor, due to its long-lived plateau. All others are averaged out in increasing proportion as bin width increases. Events lost from a contaminated template are equally recovered with baseline estimation done via iterative median sampling and by averaging 500 days of photometry.

effects of template contamination, may also lead to unreliable statistics for upcoming population studies.

We show sample events discovered by binning in 1 day, 20 day, 50 day, and 100 day bins for each of our models in the Appendix. The shaded region indicates the bin in which a detection was made.

Because these precursors are recombination-driven, the peak of their assumed blackbody emission can be calculated from Wien's law. Assuming the recombination temperature of hydrogen to be ∼4000 K, we find a peak of ∼7200 Å, between the effective wavelengths of the LSST-*r* and LSST-*i* filters. As expected, the majority of both single-visit and binned precursors at all bin widths are detected in LSST-*r* and -*i*.

3.3. Maximizing Precursor Identification via a Local Volume Galaxy Survey

SNe detected by LSST will outnumber detected precursors 10,000 to 1. Rapid association of these transients to galaxies at well-constrained distances is essential to clarify their nature as low-luminosity transients. To explore this possibility, we query the GLADE+ (G. Dálya et al. 2022) and DECaLS Data Release 10 (A. Dey et al. 2019) catalogs for all galaxies within 800 Mpc and overlapping with LSST fields. We present the cumulative number in each catalog as a function of distance in Figure 10. We overplot the 75th percentile for the distance of detected 2020tlf-like precursors from Figure 8. We find 168 spectroscopically confirmed galaxies within the GLADE+ catalog within this distance, 1912 photometric galaxies within the GLADE+ catalog, and 5090 photometric galaxies within the DECaLS DR10 catalog. Spectroscopically confirming the distances of the photometric galaxies, e.g., through The Dark Energy Spectroscopic Instrument's upcoming MOST Hosts Survey (M. T. Soumagnac et al. 2024), is critical for distinguishing new precursors from the transient zoo and further uncovering the diversity of pre-explosion variability.

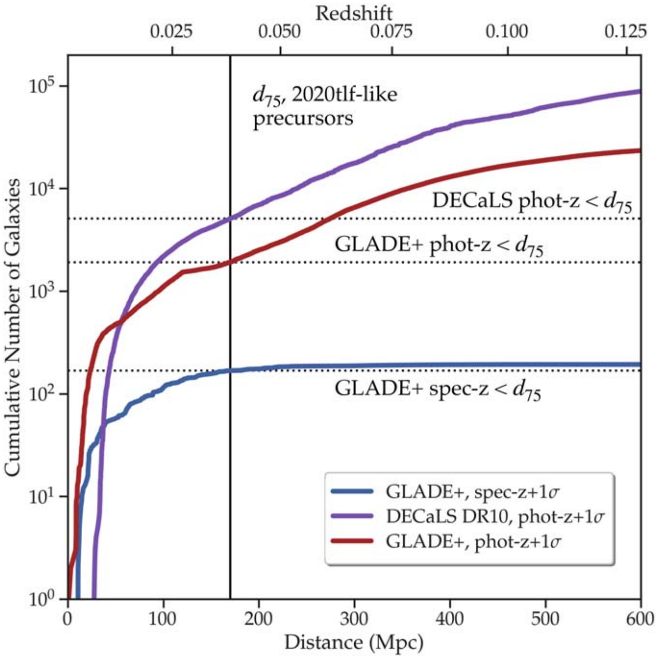

Figure 10. The cumulative number of galaxies in GLADE+ (G. Dálya et al. 2022) and DECaLS (A. Dey et al. 2019) overlapping with the LSST survey footprint as a function of distance. We show the spectroscopically confirmed GLADE+ galaxies in blue, the upper 68th phot-*z* percentile for the photometric GLADE+ galaxies in red, and the 68th phot-*z* percentile for the photometric galaxies in DECaLS DR10 in purple. Horizontal lines correspond to the cutoff distance of each catalog within which 75% of 2020tlf-like single-visit precursors are detected.

The majority of undetected events in our simulation were missed not because of the LSST survey strategy, but because of their intrinsic faintness. A higher-cadence search with smaller-aperture telescopes is unlikely to lead to additional discoveries. As a case study, we take the La Silla Schmidt Southern Survey

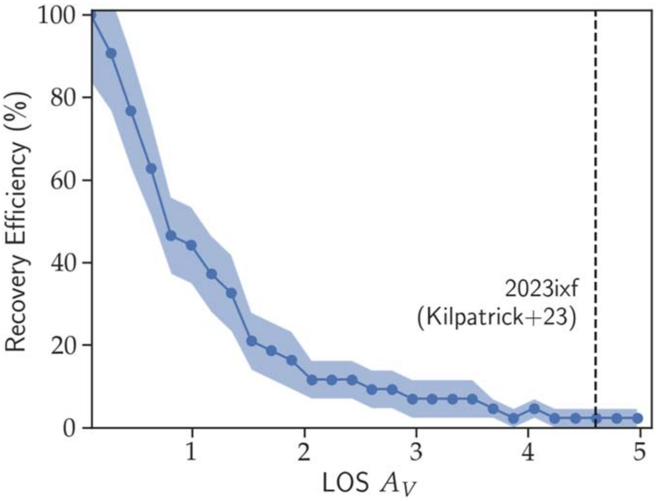

Figure 11. The recovery efficiency of 2020tlf-like precursors as a function of visual-band line-of-sight extinction A_V for a fixed volumetric rate and relative to $A_V = 0$. The shaded region gives 1σ uncertainties for each bin, and the black dashed line indicates the reported A_V value for the progenitor of SN 2023ixf from C. D. Kilpatrick et al. (2023).

(LS4) with its forecasted limiting magnitude of ∼21.[22] A coadded image of 20 background-limited LS4 exposures taken in the span between LSST observations (LS4 will observe 5000 $\deg^2$ in alternating nights between *gi* and *iz*, allowing for 20 *i*-band exposures in 20 days) will reach an apparent magnitude of ∼22.6, still magnitudes shallower than the LSST single-visit limiting magnitude of ∼24.5. BlackGEM, a wide-field Southern Hemisphere optical imager operating concurrently with LSST and with an anticipated limiting magnitude of ∼23 and a planned Local Transient Survey scanning local overdensities with six exposures per night, has greater potential for detecting additional precursors.[23] Nonetheless, photometry from smaller instruments will still be useful for *characterizing* events discovered in sparse LSST data. Our single-visit simulations recovered between 12 and 40 total precursors per year brighter than the coadded LS4 limit. Further, these surveys are useful for characterizing the photometric evolution of the most nearby CCSNe that would saturate the LSST CCDs (a transient peaking at $M < -18$within ∼60 Mpc would saturate the CCD within the anticipated 15 s exposure time),[24] as well as constraining the signatures of SN–CSM interaction. We therefore recommend a subsurvey of local galaxies to complement LSST observations and further enable this science case.

3.4. Impact of Dust on Precursor Recovery Rates

The lack of an optical detection of enhanced pre-explosion emission in the case of SN 2023ixf (C. L. Ransome et al. 2024) to an absolute magnitude limit of ~ -7, despite years-long infrared variability observed with Spitzer, suggests that dust can significantly limit the precursor yield of LSST. Detection limits of −9.5 mag were similarly obtained from pre-explosion observations of the SN 2024ggi explosion site, despite flash-ionization lines in early SN spectra suggesting the presence of local CSM (W. V. Jacobson-Galán et al. 2024a). SED modeling of the SN 2023ixf precursor was consistent with a line-of-sight extinction of $A_V \gtrsim 4.6$ mag, where the extinction is dominated by the progenitor environment. While additional limits can be derived from supernova observables, precursor emission can be obscured by substantially more dust being destroyed in the subsequent explosion. To estimate the impact that intervening dust has on precursor recovery rates, we run an additional set of 1 yr LSST simulations with the 2020tlf-like precursor model. We assume a fixed volumetric rate and increase the line-of-sight extinction parameter A_V in 27 linearly spaced bins from 0.1 to 5 mag. We report the recovery fraction in each bin in Figure 11.

The fraction of recovered events drops to $20\% \pm 7\%$ at $A_V \approx 1.5$ and $2\% \pm 2\%$ at $A_V \approx 4.6$ (the reported extinction value for the progenitor of 2023ixf; see C. D. Kilpatrick et al. 2023), dramatically limiting the demographic studies possible with LSST. At intermediate extinction values, a highly reddened precursor may allow some constraints to be placed on dust mass, but large uncertainties on composition and grain size distribution may limit the constraining power of optical photometry alone. The forthcoming Nancy G. Roman Space Telescope, which will image 2000 square degrees of the sky in four NIR filters to a depth of $J \approx 26.7$ AB during its High Latitude Wide Area Survey, will be more naturally suited to detect precursor emission from dust-enshrouded progenitors and reconstruct a warm dust SED.

4. Conclusions

In this work, we have explored the anticipated discovery rates of eruptive precursors to CCSNe with the upcoming Rubin Observatory LSST. Our key findings are summarized below.

1. Our models suggest that 40–130 eruptive precursors to SNe IIP/IIL, and ∼110 eruptive precursors to SNe IIn, will be detectable in single-visit LSST photometry annually. This recombination-powered emission will primarily occur in the *r* and *i* bands. These rates are strongly dependent on our assumed model: longer-lived and substantially brighter SN IIn precursors have been reported in the literature (N. L. Strotjohann et al. 2021) than can be explained by the IIn model outlined here, which will further increase detection rates.
2. Assuming that the template for difference imaging contains zero flux, we anticipate ∼400 SN IIn precursors by binning single-passband LSST photometry in 20 day bins and ∼250 2020tlf-like precursors binning in 100 day bins in the first three years of LSST. If IIP/IIL precursors are brighter and shorter-lived than the archetypal 2020tlf precursor, as is modeled with the MM22/II eruptions, more may be detectable in the same period.
3. When the data are binned, the DDF survey is expected to roughly double the median depth at which eruptive precursors to SNe IIP/IIL are detected relative to the primary WFD survey.
4. Line-of-sight extinction from a dusty CSM can significantly reduce the fraction of recovered precursors with optical photometry, with ∼0 events recovered at the reported extinction of the 2023ixf progenitor.
5. Despite the low number of single-visit events detected relative to other models, 2020tlf-like precursors will be prime targets for spectroscopic follow-up, due to their long duration and high number of LSST detections.

---

[22] https://www.snowmass21.org/docs/files/summaries/CF/SNOWMASS21CF6CF4PeterNugent171.pdf

[23] https://astro.ru.nl/blackgem/?page_id=302

[24] https://www.lsst.org/sites/default/files/docs/sciencebook/SB_3.pdf

6. Spectroscopic confirmation of precursor host galaxies will be critical to distinguish these rare transients from more distant events, although they will still be easily confused with luminous red novae. Complementary photometric surveys will allow for greater characterization of local CCSNe, offering the possibility of linking detected precursors to the post-explosion behavior of the SN.

Our similar LSST discovery rates between SN IIP/IIL and SN IIn precursors at first seem discrepant with observed precursor detections, which are overwhelmingly associated with SNe IIn. This result is a reflection of the significantly higher volumetric rate of SNe IIP/IIL and their dimmer modeled precursors, such that a greater fraction of events may be detectable only with the Rubin Observatory. Dedicated searches for this hidden population will significantly improve predicted event rates and characteristics.

A full treatment of eruptive precursors to CCSNe would model both phenomena simultaneously and self-consistently. Though this approach has been undertaken for individual events (e.g., 2021qqp; D. Hiramatsu et al. 2024), we have avoided imposing assumptions about the phases at which these eruptions occur in this work. Future simulations could include an associated SN using the CSM masses derived from precursor events, and investigate correlations in SN properties. Another extension to this work would be to model the dust produced during precursor episodes and link the line-of-sight extinction to the ejecta mass—although, as has been mentioned in Section 3.4, this requires imposing additional model assumptions.

We have considered single-visit and binned precursors separately, but LSST detections of a precursor in the alert stream will prompt binned searches to recover additional observations. This will be possible only for a subset of high-cadence WFD observations for precursors that evolve according to our theoretical models, or for the bulk of observations for longer-lived 2020tlf-like emission. The discovery of an associated SN will aid in selecting specific pre-explosion phases for these more targeted precursor searches.

The number of annual CCSNe within 800 Mpc is low enough that binned searches for pre-explosion emission at every site should be attempted; nonetheless, this represents a major computational undertaking, and support from International Data Access Centers (IDACs) associated with the Rubin Observatory would greatly facilitate this search.[25] Where comprehensive searches are not possible, triaged searches preceding SNe with clear signatures of CSM interaction could be prioritized, although this will severely limit the inferences that could be made about the population at large.

The number of proposed models for precursor emission continues to grow. Recently, D. Tsuna et al. (2024b) proposed a mechanism by which super-Eddington accretion from a stripped low-mass He primary onto a compact companion drives outflows that power a long-duration transient. The bolometric luminosity of this precursor (with variations from the geometry of the outflows) is constant for years prior to the destruction of the system (via either core collapse or merger), and brightens to $\sim 10^{41}$ erg s^{-1} in its final months. This model has been invoked to explain the long-lived precursor emission in the SN Ibn 20203fyq. While we only consider eruptive mass loss from hydrogen-rich progenitors in this work, this model will be the focus of a follow-up study. In another recent model, weak shock waves from an RSG interacting with an extended chromosphere are proposed to explain mass-loss rates derived for SN IIP/IIL progenitors (which are argued to probe winds driven by radiation pressure at the dust formation radius; J. Fuller & D. Tsuna 2024). A dearth of optical precursors detected in LSST data would lend support for this theory.

Although we have explored binning strategies when there are multiple eruptions preceding a single SN, we have not explicitly modeled the SED that arises from interacting shells of ejected CSM. A multi-eruption model of this kind was explored in D. Tsuna et al. (2023), and a single-eruption model was also introduced using radiation hydrodynamics. These RSG precursors last hundreds of days, significantly longer than any of the models considered in this work, and peak in the infrared at approximately the luminosity of the 2020tlf-like precursor. Extrapolating the results from our 2020tlf-like results, we expect more optimistic recovery statistics for these events when binning >100 day photometry in LSST-Y and higher median distances from events in the Deep Drilling Fields. A systematic comparison between the estimates reported here and the precursors observed in the early years of LSST will shed additional light on the physical mechanisms driving terminal mass loss in SN IIn and SN IIP/IIL progenitors.

Acknowledgments

We thank Itai Linial, Conor Ransome, and Daichi Tsuna for helpful conversations that improved this manuscript. We further acknowledge the anonymous referee for providing a constructive review. This work is supported by the National Science Foundation under Cooperative Agreement PHY-2019786 (The NSF AI Institute for Artificial Intelligence and Fundamental Interactions, http://iaifi.org/). The Villar Astro Time Lab acknowledges support through the David and Lucile Packard Foundation, National Science Foundation under AST-2433718, AST-2407922 and AST-2406110, as well as an Aramont Fellowship for Emerging Science Research.

The Legacy Surveys consist of three individual and complementary projects: DECaLS (Proposal ID #2014B-0404; PIs: David Schlegel and Arjun Dey), the Beijing–Arizona Sky Survey (BASS; NOAO Prop. ID #2015A-0801; PIs: Zhou Xu and Xiaohui Fan), and the Mayall z-band Legacy Survey (MzLS; Prop. ID #2016A-0453; PI: Arjun Dey). DECaLS, BASS, and MzLS together include data obtained, respectively, at the Blanco telescope, Cerro Tololo Inter-American Observatory, NSF's NOIRLab; the Bok telescope, Steward Observatory, University of Arizona; and the Mayall telescope, Kitt Peak National Observatory, NOIRLab. Pipeline processing and analyses of the data were supported by NOIRLab and the Lawrence Berkeley National Laboratory (LBNL). The Legacy Surveys project is honored to be permitted to conduct astronomical research on Iolkam Du'ag (Kitt Peak), a mountain with particular significance to the Tohono O'odham Nation.

NOIRLab is operated by the Association of Universities for Research in Astronomy under a cooperative agreement with the National Science Foundation. LBNL is managed by the Regents of the University of California under contract to the U.S. Department of Energy.

This project used data obtained with the Dark Energy Camera, which was constructed by the Dark Energy Survey (DES) collaboration. Funding for the DES Projects has been provided by the U.S. Department of Energy, the U.S. National Science Foundation, the Ministry of Science and Education of

---

[25] https://www.lsst.org/scientists/in-kind-program/computing-resources

Spain, the Science and Technology Facilities Council of the United Kingdom, the Higher Education Funding Council for England, the National Center for Supercomputing Applications at the University of Illinois at Urbana-Champaign, the Kavli Institute of Cosmological Physics at the University of Chicago, Center for Cosmology and Astro-Particle Physics at the Ohio State University, the Mitchell Institute for Fundamental Physics and Astronomy at Texas A&M University, Financiadora de Estudos e Projetos, Fundacao Carlos Chagas Filho de Amparo, Financiadora de Estudos e Projetos, Fundacao Carlos Chagas Filho de Amparo a Pesquisa do Estado do Rio de Janeiro, Conselho Nacional de Desenvolvimento Cientifico e Tecnologico and the Ministerio da Ciencia, Tecnologia e Inovacao, the Deutsche Forschungsgemeinschaft and the Collaborating Institutions in the Dark Energy Survey. The Collaborating Institutions are Argonne National Laboratory, the University of California at Santa Cruz, the University of Cambridge, Centro de Investigaciones Energeticas, Medioambientales y Tecnologicas-Madrid, the University of Chicago, University College London, the DES-Brazil Consortium, the University of Edinburgh, the Eidgenossische Technische Hochschule Zurich, Fermi National Accelerator Laboratory, the University of Illinois at Urbana-Champaign, the Institut de Ciencies de l'Espai, the Institut de Fisica d'Altes Energies, Lawrence Berkeley National Laboratory, the Ludwig Maximilians Universitat Munchen and the associated Excellence Cluster Universe, the University of Michigan, NSF's NOIRLab, the University of Nottingham, the Ohio State University, the University of Pennsylvania, the University of Portsmouth, SLAC National Accelerator Laboratory, Stanford University, the University of Sussex, and Texas A&M University.

BASS is a key project of the Telescope Access Program, which has been funded by the National Astronomical Observatories of China, the Chinese Academy of Sciences (the Strategic Priority Research Program "The Emergence of Cosmological Structures" Grant # XDB09000000), and the Special Fund for Astronomy from the Ministry of Finance. The BASS is also supported by the External Cooperation Program of Chinese Academy of Sciences (Grant #114A11KYSB20160057), and the Chinese National Natural Science Foundation (Grant #12120101003, #11433005).

The Legacy Survey team makes use of data products from the Near-Earth Object Wide-field Infrared Survey Explorer (NEOWISE), which is a project of the Jet Propulsion Laboratory/California Institute of Technology. NEOWISE is funded by the National Aeronautics and Space Administration.

The Photometric Redshifts for the Legacy Surveys catalog used in this paper was produced thanks to funding from the U.S. Department of Energy Office of Science, Office of High Energy Physics via grant DE-SC0007914.

The Legacy Surveys imaging of the DESI footprint is supported by the Director, Office of Science, Office of High Energy Physics of the U.S. Department of Energy under Contract No. DE-AC02-05CH1123, by the National Energy Research Scientific Computing Center, a DOE Office of Science User Facility under the same contract; and by the U.S. National Science Foundation, Division of Astronomical Sciences under Contract No. AST-0950945 to NOAO.

This work has received funding from the European Research Council under the European Union's Horizon 2020 research and innovation program (grant agreement No. 945806) and is supported by the Deutsche Forschungsgemeinschaft (German Research Foundation) under Germany's Excellence Strategy EXC 2181/1-390900948 (the Heidelberg STRUCTURES Excellence Cluster).

Software: Astropy (Astropy Collaboration et al. 2013, 2018, 2022), Matplotlib (J. D. Hunter 2007), MESA (B. Paxton et al. 2011, 2013, 2015, 2018, 2019), Numpy (C. R. Harris et al. 2020), Pandas (pandas development team 2024), Seaborn (M. Waskom 2021), Scipy (P. Virtanen et al. 2020), SNANA (R. Kessler et al. 2009).

Appendix

In Figure 12, we provide examples of precursor events across each of our four assumed models (MM22/IIn, MM22/II, L21/II, and 2020tlf-like) with photometry detected at $\geq 5\sigma$ in 1–100 day bins and assuming uncontaminated templates.

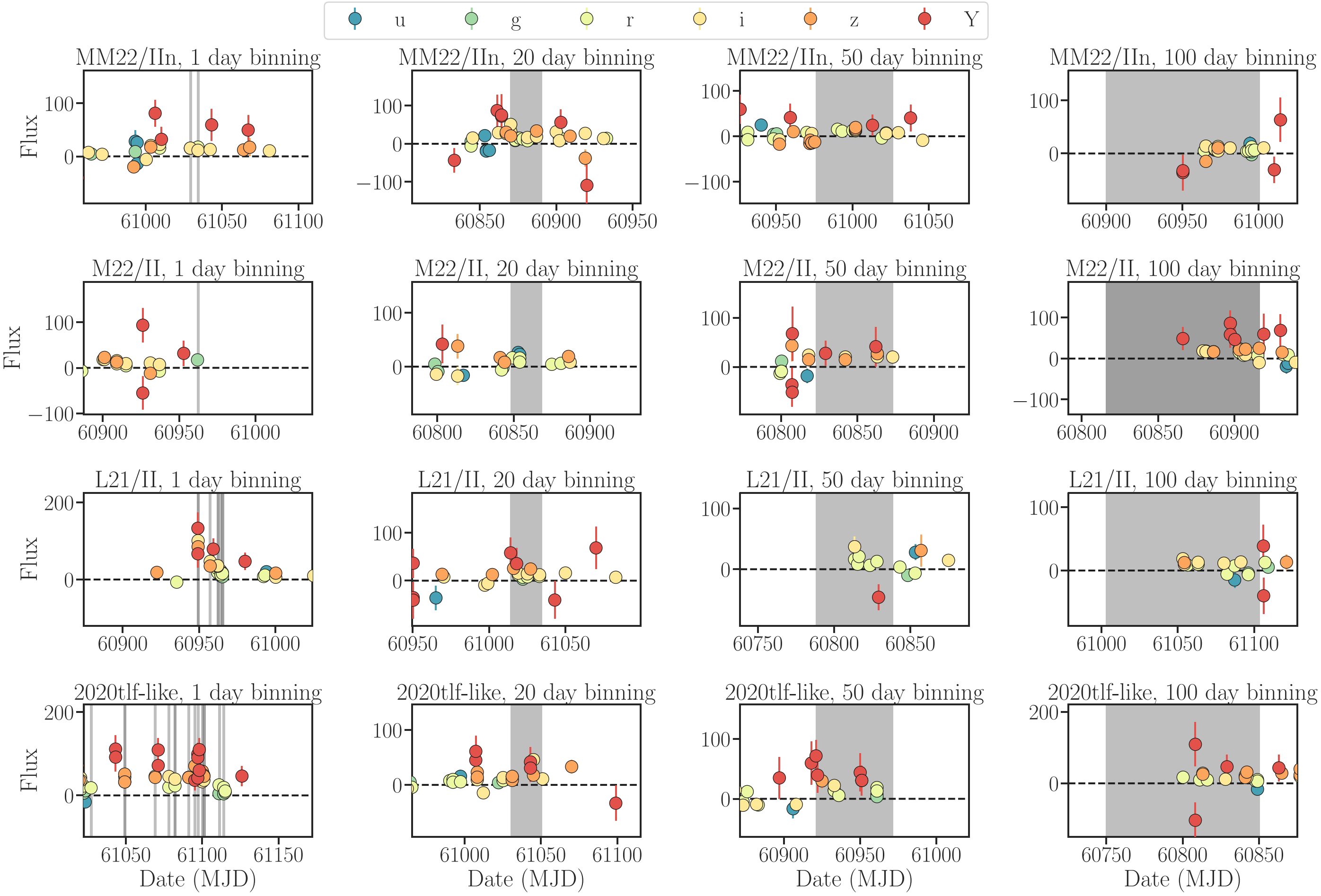

Figure 12. Examples of binned precursor events with at least one 5σ detection for each model (rows) and bin width (columns), considering both WFD and DDF observations. Each bin in which a 5σ detection was made (in any band) is shaded. Most detections are made in LSST-*r* and LSST-*i*.

ORCID iDs

A. Gagliano https://orcid.org/0000-0003-4906-8447
E. Berger https://orcid.org/0000-0002-9392-9681
V. A. Villar https://orcid.org/0000-0002-5814-4061
D. Hiramatsu https://orcid.org/0000-0002-1125-9187
R. Kessler https://orcid.org/0000-0003-3221-0419
T. Matsumoto https://orcid.org/0000-0002-9350-6793
A. Gilkis https://orcid.org/0000-0001-8949-5131
E. Laplace https://orcid.org/0000-0003-1009-5691

References

Aleo, P. D., Malanchev, K., Sharief, S., et al. 2023, ApJS, 266, 9
Astropy Collaboration, Price-Whelan, A. M., Lim, P. L., et al. 2022, ApJ, 935, 167
Astropy Collaboration, Price-Whelan, A. M., Sipőcz, B. M., et al. 2018, AJ, 156, 123
Astropy Collaboration, Robitaille, T. P., Tollerud, J. E., et al. 2013, A&A, 558, A33
Bellm, E. C., Kulkarni, S. R., Graham, M. J., et al. 2019, PASP, 131, 018002
Berger, E., Foley, R., & Ivans, I. 2009, ATel, 2184, 1
Biswas, R., Daniel, S. F., Hložek, R., et al. 2020, ApJS, 247, 60
Brennan, S. J., Sollerman, J., Irani, I., et al. 2024, A&A, 684, L18
Cold, C., & Hjorth, J. 2023, A&A, 670, A48
Dálya, G., Díaz, R., Bouchet, F. R., et al. 2022, MNRAS, 514, 1403
Davis, K. W., Taggart, K., Tinyanont, S., et al. 2023, MNRAS, 523, 2530
Dekany, R., Smith, R. M., Riddle, R., et al. 2020, PASP, 132, 038001
Dey, A., Schlegel, D. J., Lang, D., et al. 2019, AJ, 157, 168
Dong, Y., Tsuna, D., Valenti, S., et al. 2024, arXiv:2405.04583
Drake, A. J., Howerton, S., McNaught, R., et al. 2012, ATel, 4334, 1
Elias-Rosa, N., Brennan, S. J., Benetti, S., et al. 2024, A&A, 686, A13
Filippenko, A. V. 1997, ARA&A, 35, 309
Foley, R. J., Berger, E., Fox, O., et al. 2011, ApJ, 732, 32
Foley, R. J., Smith, N., Ganeshalingam, M., et al. 2007, ApJL, 657, L105
Forster, F., Moriya, T. J., Maureira, J. C., et al. 2018, NatAs, 2, 808
Fraser, M. 2020, RSOS, 7, 200467
Fuller, J., & Tsuna, D. 2024, OJAp, 7, 47
Gal-Yam, A., Bruch, R., Schulze, S., et al. 2022, Natur, 601, 201
Gal-Yam, A., & Leonard, D. C. 2009, Natur, 458, 865
Gangopadhyay, A., Misra, K., Hiramatsu, D., et al. 2020, ApJ, 889, 170
Gilkis, A., & Arcavi, I. 2022, MNRAS, 511, 691
Goldberg, J. A., & Bildsten, L. 2020, ApJL, 895, L45
Graham, M. J., Kulkarni, S. R., Bellm, E. C., et al. 2019, PASP, 131, 078001
Graham, M. L., Sand, D. J., Valenti, S., et al. 2014, ApJ, 787, 163
Hachinger, S., Mazzali, P. A., Taubenberger, S., et al. 2012, MNRAS, 422, 70
Harris, C. R., Millman, K. J., van der Walt, S. J., et al. 2020, Natur, 585, 357
Heger, A., Jeannin, L., Langer, N., & Baraffe, I. 1997, A&A, 327, 224
Hiramatsu, D., Matsumoto, T., Berger, E., et al. 2024, ApJ, 964, 181
Hunter, J. D. 2007, CSE, 9, 90
Jacobson-Galán, W. V., Davis, K. W., Kilpatrick, C. D., et al. 2024a, ApJ, 972, 177
Jacobson-Galán, W. V., Dessart, L., Davis, K. W., et al. 2024b, ApJ, 970, 189
Jacobson-Galán, W. V., Dessart, L., Jones, D. O., et al. 2022, ApJ, 924, 15
Jones, D. O., Foley, R. J., Narayan, G., et al. 2021, ApJ, 908, 143
Ivezić, Ž., Kahn, S. M., Tyson, J. A., et al. 2019, ApJ, 873, 111
Kasliwal, M. M. 2013, in IAU Symp. 281, Binary Paths to Type Ia Supernovae Explosions, ed. R. Di Stefano, M. Orio, & M. Moe (Cambridge: Cambridge Univ. Press), 9
Kessler, R., Bernstein, J. P., Cinabro, D., et al. 2009, PASP, 121, 1028
Kessler, R., Narayan, G., Avelino, A., et al. 2019, PASP, 131, 094501

Kilpatrick, C. D., Foley, R. J., Jacobson-Galán, W. V., et al. 2023, ApJL, 952, L23
Kuriyama, N., & Shigeyama, T. 2021, A&A, 646, A118
Laplace, E., Justham, S., Renzo, M., et al. 2021, A&A, 656, A58
Linial, I., Fuller, J., & Sari, R. 2021, MNRAS, 501, 4266
LSST Dark Energy Science Collaboration (LSST DESC), Abolfathi, B., & Alonso, D. 2021, ApJS, 253, 31
Maeda, K., & Moriya, T. J. 2022, ApJ, 927, 25
Mahy, L., Lanthermann, C., Hutsemékers, D., et al. 2022, A&A, 657, A4
Margutti, R., Milisavljevic, D., Soderberg, A. M., et al. 2014, ApJ, 780, 21
Masci, F. J., Laher, R. R., Rusholme, B., et al. 2019, PASP, 131, 018003
Matsumoto, T., & Metzger, B. D. 2022a, ApJ, 936, 114
Matsumoto, T., & Metzger, B. D. 2022b, ApJ, 938, 5
Matsuoka, T., & Sawada, R. 2024, ApJ, 963, 105
Mauerhan, J. C., Smith, N., Filippenko, A. V., et al. 2013a, MNRAS, 430, 1801
Mauerhan, J. C., Smith, N., Silverman, J. M., et al. 2013b, MNRAS, 431, 2599
Muller, B., Heger, A., Liptai, D., & Cameron, J. B. 2016, MNRAS, 460, 742
Nagao, T., Kuncarayakti, H., Maeda, K., et al. 2023, A&A, 673, A27
Ofek, E. O., Sullivan, M., Cenko, S. B., et al. 2013, Natur, 494, 65
Ofek, E. O., Sullivan, M., Shaviv, N. J., et al. 2014, ApJ, 789, 104
pandas development team, T 2024, pandas-dev/pandas: Pandas, v2.2.2, Zenodo, doi:10.5281/zenodo.10957263
Pastorello, A., Cappellaro, E., Inserra, C., et al. 2013, ApJ, 767, 1
Pastorello, A., Kochanek, C. S., Fraser, M., et al. 2018, MNRAS, 474, 197
Pastorello, A., Mason, E., Taubenberger, S., et al. 2019, A&A, 630, A75
Pastorello, A., Smartt, S. J., Mattila, S., et al. 2007, Natur, 447, 829
Paxton, B., Bildsten, L., Dotter, A., et al. 2011, ApJS, 192, 3
Paxton, B., Cantiello, M., Arras, P., et al. 2013, ApJS, 208, 4
Paxton, B., Marchant, P., Schwab, J., et al. 2015, ApJS, 220, 15
Paxton, B., Schwab, J., Bauer, E. B., et al. 2018, ApJS, 234, 34
Paxton, B., Smolec, R., Schwab, J., et al. 2019, ApJS, 243, 10
Pellegrino, C., Howell, D. A., Terreran, G., et al. 2022, ApJ, 938, 73
Pursiainen, M., Leloudas, G., Schulze, S., et al. 2023, ApJL, 959, L10
Quataert, E., & Shiode, J. 2012, MNRAS, 423, L92
Ransome, C. L., Villar, V. A., Tartaglia, A., et al. 2024, ApJ, 965, 93
Reguitti, A., Pignata, G., Pastorello, A., et al. 2024, A&A, 686, A231
Sakurai, A. 1960, Commun. Pur. Appl. Math., 13, 353
Sana, H., de Mink, S. E., de Koter, A., et al. 2012, Sci, 337, 444
Sánchez, B. O., Kessler, R., Scolnic, D., et al. 2022, ApJ, 934, 96
Schlegel, E. M. 1990, MNRAS, 244, 269
Sedov, L. I. 1946, JApMM, 10, 241
Shappee, B. J., Prieto, J. L., Grupe, D., et al. 2014, ApJ, 788, 48
Shiode, J. H., & Quataert, E. 2014, ApJ, 780, 96
Shivvers, I., Modjaz, M., Zheng, W., et al. 2017, PASP, 129, 054201
Shrestha, M., Bostroem, K. A., Sand, D. J., et al. 2024, ApJL, 972, L15
Smith, N. 2013, MNRAS, 434, 102
Smith, N. 2014, ARA&A, 52, 487
Smith, N. 2017, in Handbook of Supernovae, ed. A. W. Alsabti & P. Murdin (Cham: Springer), 403
Smith, N., Miller, A., Li, W., et al. 2010, AJ, 139, 1451
Soumagnac, M. T., Nugent, P., Knop, R. A., et al. 2024, ApJS, 275, 22
Strolger, L.-G., Dahlen, T., Rodney, S. A., et al. 2015, ApJ, 813, 93
Strotjohann, N. L., Ofek, E. O., Gal-Yam, A., et al. 2021, ApJ, 907, 99
Sun, N.-C., Maund, J. R., Hirai, R., Crowther, P. A., & Podsiadlowski, P. 2020, MNRAS, 491, 6000
Taddia, F., Stritzinger, M. D., Sollerman, J., et al. 2013, A&A, 555, A10
Tartaglia, L., Pastorello, A., Sullivan, M., et al. 2016, MNRAS, 459, 1039
Thöne, C. C., de Ugarte Postigo, A., Leloudas, G., et al. 2017, A&A, 599, A129
Tonry, J. L., Denneau, L., Heinze, A. N., et al. 2018, PASP, 130, 064505
Tsuna, D., Matsumoto, T., Wu, S. C., & Fuller, J. 2024a, ApJ, 966, 30
Tsuna, D., Takei, Y., & Shigeyama, T. 2023, ApJ, 945, 104
Tsuna, D., Wu, S. C., Fuller, J., Dong, Y., & Piro, A. L. 2024b, OJAp, 7, 82
Tsvetkov, D. Y., Volnova, A. A., Shulga, A. P., et al. 2006, A&A, 460, 769
Vanbeveren, D., De Loore, C., & Van Rensbergen, W. 1998, A&ARv, 9, 63
Virtanen, P., Gommers, R., Oliphant, T. E., et al. 2020, NatMe, 17, 261
Wang, Q., Goel, A., Dessart, L., et al. 2024, MNRAS, 530, 3906
Waskom, M. 2021, JOSS, 6, 3021
Woosley, S. E. 2019, ApJ, 878, 49
Xiang, D., Mo, J., Wang, X., et al. 2024, ApJL, 969, L15
Yoon, S.-C., & Cantiello, M. 2010, ApJL, 717, L62